

Article

Evaluation of Satellite-Altimetry-Derived Pycnocline Depth Products in the South China Sea

Yingying Chen ^{1,2}, Kai Yu ^{1,3} , Changming Dong ^{1,4}, Zhigang He ⁵, Yunwei Yan ³
and Dongxiao Wang ^{2,*}

¹ School of Marine Science, Nanjing University of Information Science and Technology, Nanjing 210044, China; cyy@scsio.ac.cn (Y.C.); yukai041@nuist.edu.cn (K.Y.); cmdong@gmail.com (C.D.)

² State Key Laboratory of Tropical Oceanography, South China Sea Institute of Oceanology, Chinese Academy of Sciences, Guangzhou 510000, China

³ State Key Laboratory of Satellite Ocean Environment Dynamics, Second Institute of Oceanography, State Oceanic Administration, Hangzhou 310000, China; yanyunwei@sio.org.cn

⁴ Department of Atmospheric and Oceanic Sciences, University of California, Los Angeles, CA 90095, USA

⁵ College of Ocean and Earth Science, Xiamen University, Xiamen 361000, China; zghe@xmu.edu.cn

* Correspondence: dxwang@scsio.ac.cn; Tel.: +86-18-664-692-695

Received: 27 June 2017; Accepted: 8 August 2017; Published: 12 August 2017

Abstract: The climatological monthly gridded World Ocean Atlas 2013 temperature and salinity data and satellite altimeter sea level anomaly data are used to build two altimeter-derived high-resolution real-time upper layer thickness products based on a highly simplified two-layer ocean model of the South China Sea. One product uses the proportional relationship between the sea level anomaly and upper layer thickness anomaly. The other one adds a modified component (η'_M) to account for the barotropic and thermodynamic processes that are neglected in the former product. The upper layer thickness, in this work, represents the depth of the main pycnocline, which is defined as the thickness from the sea surface to the 25 kg/m³ isopycnal depth. The mean upper layer thickness in the semi-closed South China Sea is ~120 m and the mean reduced gravity is ~0.073 m/s², which is about one order of magnitude larger than the value obtained in the open deep ocean. The long-term temperature observations from three moored buoys, the conductivity-temperature-depth profiles from three joint cruises, and the Argo measurements from 2006 to 2015 are used to compare and evaluate these two upper layer thickness products. It shows that adding the η'_M component is necessary to simulate the upper layer thickness in some situations, especially in summer and fall in the northern South China Sea.

Keywords: upper layer thickness; satellite altimeter; two-layer ocean model; South China Sea

1. Introduction

The development of satellite remote sensing technology has enabled the retrieval of high-resolution, real-time, global information on the ocean. However, remote sensors can only “see” the sea surface. To infer underwater information using remote sensing data, one of the simplest and most used ways is to use the two-layer ocean model [1]. This model simplifies the stratified ocean to a two-layer homogeneous fluid, regarding the main pycnocline as the interface and the main pycnocline depth as the upper layer thickness (ULT). With the two-layer ocean model, one can easily derive the ULT, and the barotropic mode and first baroclinic mode of the circulation using satellite altimeter sea level anomaly (SLA) data.

The altimeter-derived ULT and circulation products are widely used in various areas for different purposes. Garzoli et al. [2] monitored the upper layer transport in the southeastern Atlantic Ocean; Sainz-Trapaga et al. [3] identified the Kuroshio Extension, its bifurcation, and its northern branch;

Goni and Wainer [4] investigated the variability of the Brazil Current front. After adding satellite sea surface temperature (SST) data to the two-layer ocean model, Shay et al. [5] estimated upper layer thermal structure and upper layer heat content, and then studied the effects of a warm oceanic feature associated with Hurricane Opal. Following Shay et al. [5], Pun et al. [6] improved typhoon intensity forecasts and analyzed the spatial and temporal errors in the western North Pacific Ocean with the satellite-derived upper layer heat content. Vertical thermal structure and upper-ocean heat content from satellite remote sensing data had also been obtained by combining climatological hydrographic data and the two-layer ocean model (e.g., [7–9]). Most of the studies mentioned above were for the open ocean. Lin et al. [10] were the first to use altimeter data and the two-layer ocean model to study the spatial and temporal variation of ULT in the semi-closed South China Sea.

The SLA changes through mainly three processes: barotropic motions, the vertical Ekman pumping of the main pycnocline and the near-surface density flux above the seasonal pycnocline [11]. The Ekman pumping of the main pycnocline is the most important process, and the other two are usually one order of magnitude smaller than that of the main pycnocline fluctuations in the open ocean. The altimeter-derived ULT product based on the two-layer ocean model is mainly dependent on the proportional relationship between the SLA and main pycnocline fluctuations. As with previous studies in the open ocean, the effects of barotropic motions and near-surface density flux on the variability of SLA were not discussed in the work of Lin et al. [10]. However, these factors may play a more important role in the semi-closed South China Sea. The South China Sea is the largest marginal sea in the Northwest Pacific. Its mean depth is ~1200 m and maximum depth is ~5000 m, with a diamond-shaped deep basin oriented along the northeast-southwest direction (Figure 1). The SLA and upper layer circulation in the South China Sea have strong seasonal variability that is primarily driven by the monsoon wind [12–14]. The coastal regions show a higher seasonal sea level cycle than deep water (e.g., [15,16]). Liu et al. [17] found that the seasonal variability of the SLA is forced mainly by surface wind curl, and secondarily (about 20%) by surface net heat flux. They concluded that the surface net heat flux can obviously change the seasonal variability of the SLA, especially in the central South China Sea, by expanding/contracting the water column in the mixed layer, and the influence of the surface net heat flux is much stronger than for the open ocean. Cheng and Qi [18] argued that on seasonal time scales the baroclinic component to a great extent explains the SLA over the deep part of the South China Sea basin, whereas the barotropic component has a significant contribution to the SLA over shallow water areas in the South China Sea.

In the present study, instead of the historical ocean profiles, the gridded data is used to derive the altimeter-derived ULT products in the South China Sea. We first get the high-resolution ($0.25^\circ \times 0.25^\circ$) altimeter-derived ULT products and give a comprehensive assessment of the ULT products with multifarious in situ observations. A monthly varied modified component is first introduced into the two-layer ocean model to examine the effects of the barotropic component and near-surface density flux on the ULT products in the South China Sea. This paper is organized as follows: Section 2 describes the data. Section 3 introduces the methodology. Section 4 determines the product parameters. Section 5 evaluates the products with different in situ datasets. Section 6 discusses the physical mechanisms of the modified component. Finally, we give our conclusions and discussions in Section 7.

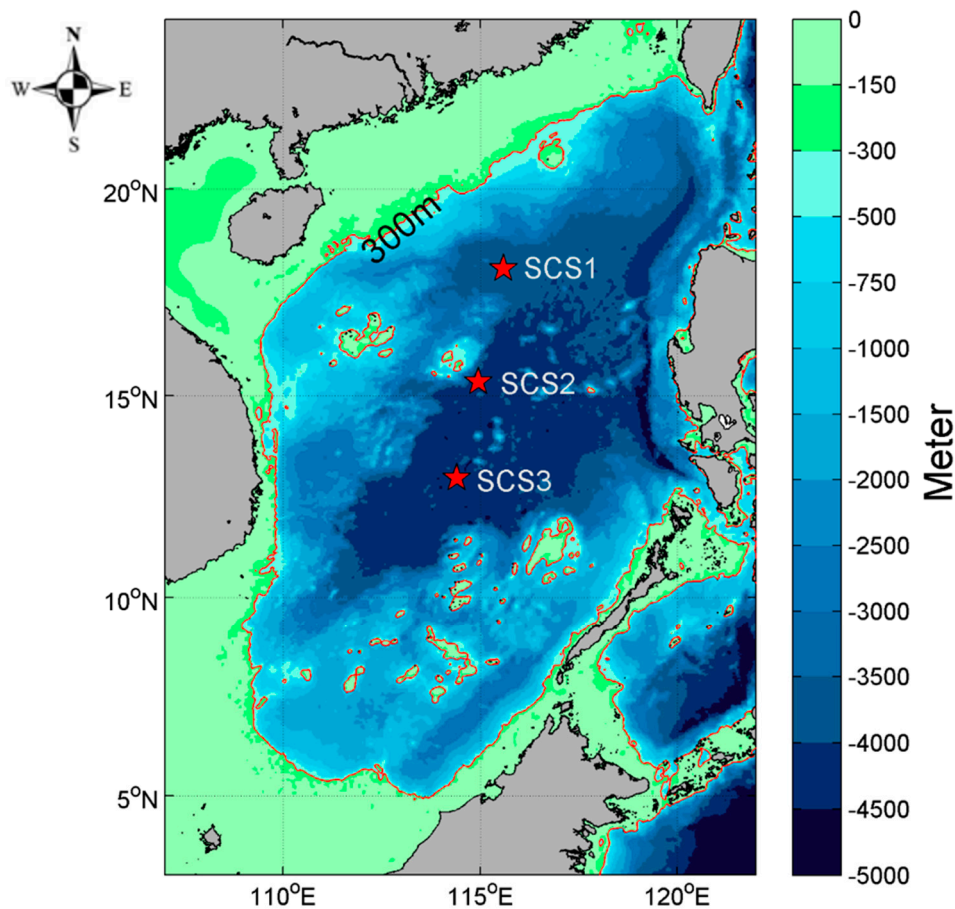


Figure 1. Bottom topography of the South China Sea. The locations of three ATLAS buoys SCS1 ($18^{\circ}5.9'N$, $115^{\circ}35.8'E$), SCS2 ($15^{\circ}20.6'N$, $114^{\circ}57.3'E$), SCS3 ($12^{\circ}58.5'N$, $114^{\circ}24.5'E$) are indicated by red stars.

2. Data

Two datasets are used to derive the ULT product in the South China Sea. The first is the climatological monthly temperature and salinity data at standard depth levels with a horizontal resolution of 0.25° both in longitude and latitude taken from the World Ocean Atlas 2013 [19]. The second is the daily and climatological monthly delayed-time level 4 gridded SLA products from multi-satellite observation provided by Archiving, Validation and Interpretation of Satellite Oceanographic Data (AVISO [20], version 5.1). The SLA data have the same spatial resolution as the World Ocean Atlas 2013 and have been modified for various atmospheric, tidal and instrumental corrections [21,22].

Three different kinds of in situ datasets are used to validate and evaluate the ULT product. The first dataset consists of measurements from three autonomous temperature line acquisition system (ATLAS) buoys (named SCS1, SCS2 and SCS3), deployed by the Institute of Oceanography, Taiwan University during the South China Sea Monsoon Experiment, whose locations are shown in Figure 1. The temporal spans are from 17 April 1997 to 9 April 1999 for SCS1, from 11 April 1998 to 10 April 1999 for SCS2, and from 12 April 1998 to 10 April 1999 for SCS3. The temporal resolution is 10 min, and the measurement depth is 1 m, 25 m, 50 m, 75 m, 100 m, 125 m, 150 m, 200 m, 250 m, 300 m and 500 m.

The Argo measurements available in the South China Sea from 2006 to 2015 (Figure 2a) are provided by the US Global Ocean Data Assimilation Experiment (USGODAE [23]). The conductivity-temperature-depth (CTD) probe data from three joint cruises in July 1998 (from 4 June to 21 July 1998), August 2000 (from 2 August to 3 September 2000) and May 2004 (from 29 April

to 25 May 2004) are provided by the South China Sea Institute of Oceanology of the Chinese Academy of Sciences. These three cruises include 133, 189 and 143 different CTD casts, respectively (Figure 2b). These data are widely used in South China Sea studies (e.g., [24,25]).

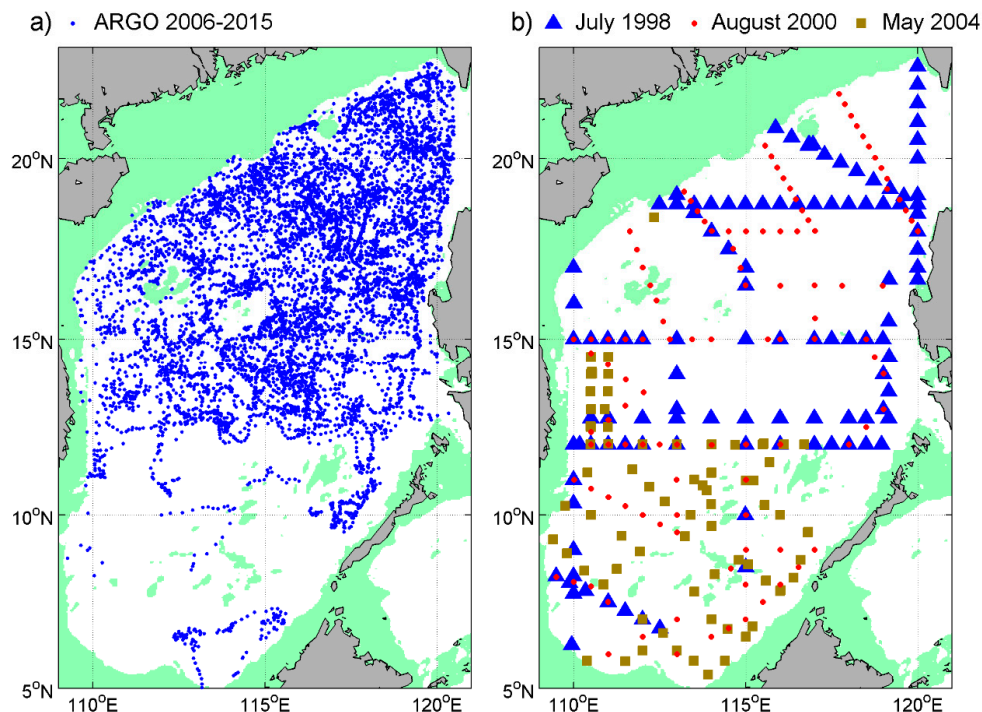


Figure 2. Distribution of (a) Argo measurements from 2006 to 2015 and (b) CTD data of three joint cruises investigation in July 1998 (blue triangles), August 2000 (red points) and May 2004 (golden squares).

3. Methods

The ocean bottom pressure (P_o) is the sum of the sea surface atmospheric pressure (P_a) and the weight per unit area of the water column:

$$P_o = P_a + g \int_{-D}^{\eta} \rho dz \quad (1)$$

where D is the mean ocean depth, η represents the sea surface height above geoid, g is the gravitational acceleration, and ρ is sea water density. According to the Boussinesq approximation, Equation (1) can be further approximated by

$$P_o = P_a + g \int_{-D}^0 \rho dz + g\rho_0\eta \quad (2)$$

where ρ_0 is the mean density of the ocean, which is equal to 1025 kg/m^3 in this study. The fluctuating ocean bottom pressure (P'_o) is caused by the variability of atmospheric pressure, the density fluctuations under the mean sea surface and the SLA (η'):

$$P'_o = P'_a + g \int_{-D}^0 \rho' dz + g\rho_0\eta' \quad (3)$$

Now η' can be partitioned into barotropic (η'_b) and steric components (η'_s):

$$\eta' = \eta'_b + \eta'_s. \quad (4)$$

The barotropic component changes as a result of internal mass redistribution in the ocean or water-mass flux, which are directly correlated with ocean bottom pressure, or changes as a result of the variability of atmospheric pressure:

$$\eta'_b = \frac{P'_a - P'_o}{g\rho_0}. \quad (5)$$

The steric component, also called the baroclinic component, changes depending on the seawater density of the water column but corresponds neither to ocean bottom pressure nor to sea surface atmospheric pressure:

$$\eta'_s = -\frac{1}{\rho_0} \int_{-D}^0 \rho' dz. \quad (6)$$

According to Gill and Niiler [11], the steric height anomaly, η'_s , is produced mainly by the variability of vertical Ekman pumping of the main pycnocline and near-surface density flux above the seasonal pycnocline.

The ocean is continuously stratified, with a sharp vertical density gradient in the pycnocline. The two-layer model, proposed by Goni et al. [1], simplifies the stratified ocean as a two-layer homogeneous fluid, regarding the main pycnocline depth as the interface. Let the thicknesses and densities of the upper and lower layer be h_1 , ρ_1 , h_2 , and ρ_2 , respectively. The sea surface height is then

$$\eta = h_1 + h_2 - D, \quad (7)$$

and the ocean bottom pressure is then

$$P_o = P_a + g\rho_1 h_1 + g\rho_2 h_2 \quad (8)$$

Combining Equations (7) and (8) yields:

$$\eta = \varepsilon h_1 + B, \quad (9)$$

where

$$\varepsilon = (\rho_2 - \rho_1)/\rho_2, \quad (10)$$

and

$$B = \frac{P_o - P_a}{g\rho_2} - D = \frac{\rho_1}{\rho_2} h_1 + h_2 - D. \quad (11)$$

The fluctuating part of Equation (9) is

$$\eta' = \varepsilon h'_1 + B'. \quad (12)$$

As one can see, B' has the same meaning as η'_b in Equation (4), and varies with the variabilities of the ocean bottom pressure and sea surface atmospheric pressure. On the other hand, the $\varepsilon h'_1$ has the same meaning as η'_s in Equation (4), and this illustrates that the steric component of the SLA in the two-layer ocean model is only caused by the fluctuations of the interface (main pycnocline). However, the effect of near-surface density flux is not considered in this model.

Generally speaking, the lower layer thickness in the deep ocean is much larger than that of the upper layer. If it is further assumed that the lower layer is infinitely deep and the fluid in the lower layer is stagnant, the model can be referred to as a 1.5-layer reduced gravity model. In the 1.5-layer reduced gravity model, the barotropic component, B' , is negligible and the SLA is equal to the baroclinic component and proportional to the ULTA anomaly (ULTA), h'_1 [3]. Letting η'_{ULT} denote the part of SLA that is proportional to the ULTA, then we have

$$\eta'(t) = \eta'_{ULT}(t) = \varepsilon h'_1(t). \quad (13)$$

As a result, the real-time ULT product can be derived from the corresponding altimeter data:

$$h_1(t) = \bar{h}_1 + h'_1(t) = \bar{h}_1 + \frac{1}{\varepsilon} \eta'(t), \quad (14)$$

where \bar{h}_1 represents the climatological mean ULT. Both \bar{h}_1 and ε can be calculated from the World Ocean Atlas 2013 data. The 1.5-layer reduced gravity model is widely used in simulating the upper-ocean circulation in the South China Sea (e.g., [26–28]).

Equation (14) only considers the proportional relationship between the SLA and ULTA. However, the barotropic and sea surface thermodynamic processes will change the SLA, while having little effect on the main pycnocline fluctuations. They will break the proportional relationship between the SLA and ULTA and bring error into the altimeter-derived ULT product based on Equation (14). To consider the effects of these processes, we add a modified component η'_M , and then η' can be divided into two parts η'_{ULT} and η'_M :

$$\eta'(t) = \eta'_{ULT}(t) + \eta'_M(t). \quad (15)$$

The climatological monthly η'_{ULT} can be derived from h'_1 based on Equation (13). The h'_1 is calculated from the World Ocean Atlas data. Then the climatological monthly η'_M can be produced by subtracting the World Ocean Atlas-derived η'_{ULT} from the η' , which is obtained from the climatological monthly altimeter data. Then the real-time ULT product can be obtained with the daily altimeter data by regarding the climatological monthly η'_M as a background field:

$$h_1(t) = \bar{h}_1 + \frac{1}{\varepsilon} \eta'_{ULT}(t) = \bar{h}_1 + \frac{1}{\varepsilon} (\eta'(t) - \eta'_M(t)). \quad (16)$$

4. Parameter Determination

To get the altimeter-derived ULT products, the first step is to determine the interface of the two-layer ocean model. Given that the effect of salinity on the density is smaller than the effect of temperature, previous investigators usually choose the depth of a certain isotherm as the interface to correspond to the main thermocline depth (e.g., [1–4]). After analyzing the in situ hydrographic data from the World Ocean Database 2005, Lin et al. [10] found the 16 °C isotherm has a better linear correlation with the SLA than those at 12 °C, 14 °C, 18 °C, or 20 °C, and thus used the depth of the 16 °C isotherm as the interface of the South China Sea. In our study, from the climatological mean temperature and density profiles over the South China Sea region derived from the World Ocean Atlas 2013 (Figure 3a), one can see that the thermocline and pycnocline depths are nearly the same in the South China Sea. Both are mainly located between 50 m and 200 m. Around this depth range, different isotherms and isopycnals depths (Figure 3a) are adopted to calculate the climatological monthly ULT and ULTA using the World Ocean Atlas 2013 data. All available spatial and temporal ULTA values in the South China Sea are compared with the corresponding SLA (Figure 3b,c). The spatial grid pixels are excluded when the water depth is shallower than 300 m (Figure 1) because of the inapplicability of the two-layer ocean model in the continental shelf area. The correlation coefficients between the SLA and ULTA reach a maximum when choosing the 20 °C isotherm or 25 kg/m³ isopycnal. Both the maximum correlation coefficients are ~0.77 and the corresponding depths of these two choices are ~120 m (Figure 3a). The strong similarity suggests that the salinity effect is weak. The 25 kg/m³ isopycnal depth will be used to represent the ULT in the remainder of this paper. The 20 °C isotherm depth is adopted to represent the ULT only when the ULT product is validated with the ATLAS buoys' data, because the ATLAS buoys lack salinity data.

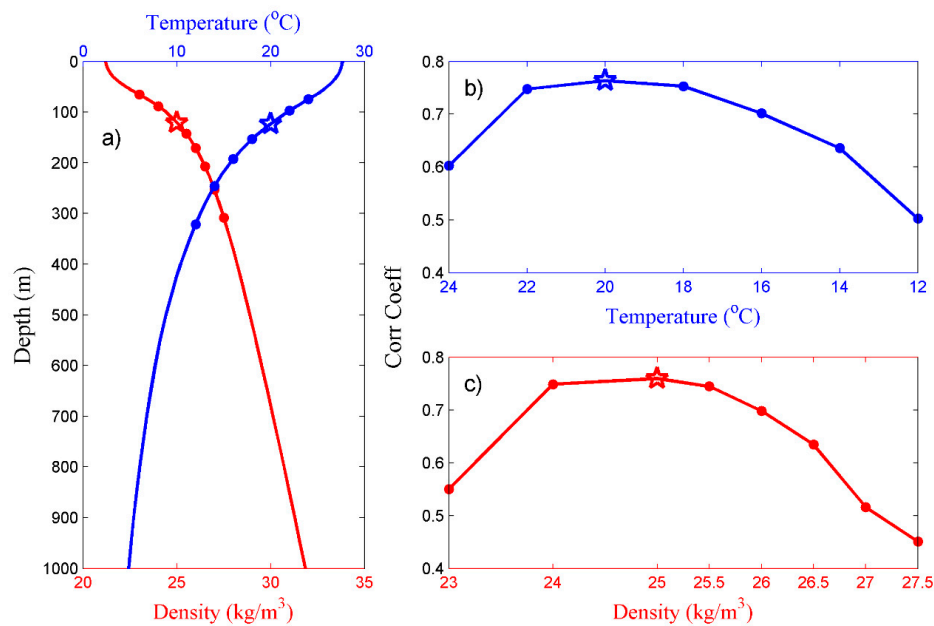


Figure 3. (a) The mean temperature (blue) and density (red) profile in the South China Sea derived from the World Ocean Atlas 2013. The correlation coefficient between the SLA and ULTA calculated by different (b) temperature and (c) density. The stars indicate where the maximum correlation coefficients appear.

Figure 4 shows the comparison of the correlation between the SLA and ULTA in different seasons. The winter, spring, summer and fall values correspond here to January, April, July and October, respectively. The correlation coefficient is high (beyond 95% t-test confidence interval) throughout the year. The mean correlation coefficient is 0.76 ± 0.07 . The maximum correlation coefficient is 0.86 which happens in spring (Figure 4b), and the minimum is 0.72 in summer (Figure 4c).

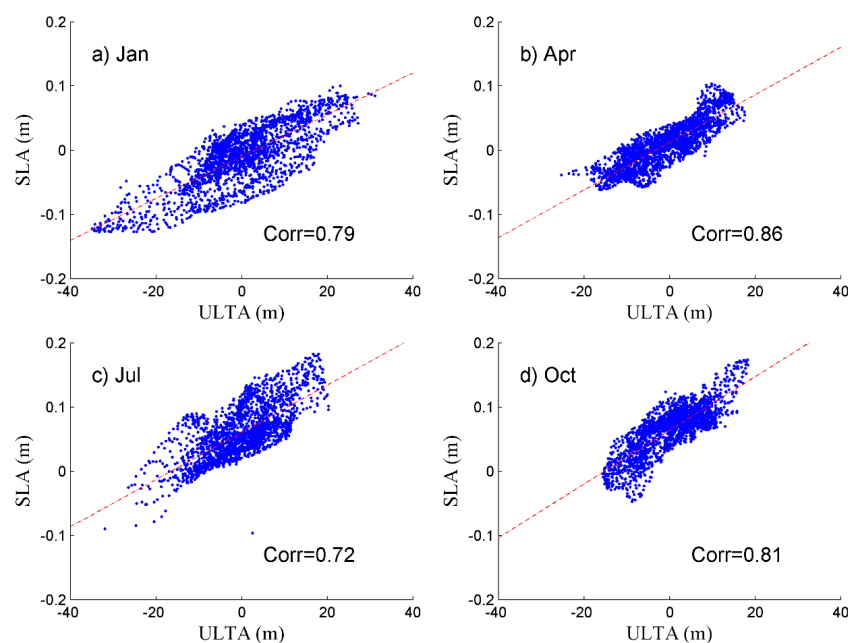


Figure 4. The scatter plots of SLA and ULTA calculated by 25 kg/m³ isopycnal in January, April, July and October (a–d). The line of best fit is represented by the red dashed line.

After determining the interface of the two-layer ocean model, the climatological mean \bar{h}_1 , ρ_1 , ρ_2 and ε can be calculated from the World Ocean Atlas 2013 data. Figure 5a illustrates the climatological mean ULT, \bar{h}_1 , in the South China Sea. The mean ULT is ~ 120 m and becomes thicker toward the east. There are two eddy-like thinner ULT areas at 18°N , 118°E and 14°N , 111°E , corresponding to the cold eddy northwest of the Luzon Island [13,29] and the cold eddy off the Vietnamese coast [27,30], respectively. Figure 5b shows that the distribution of ε in the South China Sea. ε increases gradually from the northwest to southeast South China Sea, with the values between 7.0×10^{-3} and 7.8×10^{-3} in most of our study area. For the regions near the continental shelf edge, the ε rapidly decreases to $\sim 5.0 \times 10^{-3}$. Around the Nansha Islands, ε also decreases rapidly. The reduced gravity g' can be estimated by multiplying ε by the gravitational acceleration. This gives $g' \sim 0.073$ m/s² in the South China Sea, which is about one order of magnitude larger than the value obtained in the open deep ocean (e.g., [1,2]).

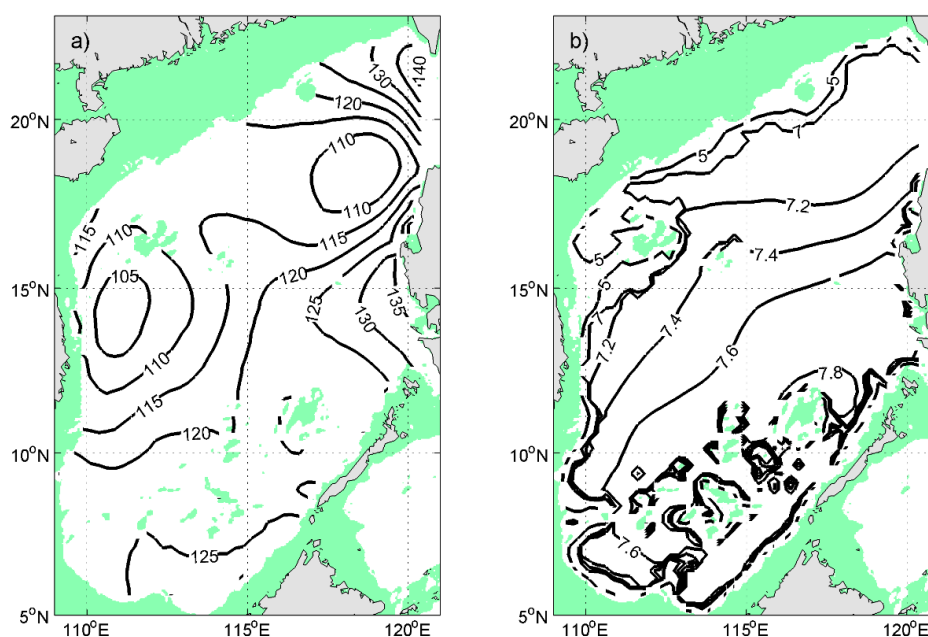


Figure 5. Climatological mean (a) ULT (CI: 5 m) and (b) ε ($\times 10^{-3}$) in the South China Sea derived from the World Ocean Atlas 2013.

The first row of Figure 6 shows the climatological seasonal variation of η' , SLA. In winter, η' is negative in most of the South China Sea, and reaches a minimum in the northeastern South China Sea. This is mainly due to the reinforcement of the cold eddy northwest of the Luzon Island. η' gradually increases in spring and reaches a maximum in the northeastern South China Sea in summer. Then η' decreases in fall and starts another cycle. The maximum seasonal variability of η' in the northeastern South China Sea suggests that the cold eddy northwest of the Luzon Island dominates the seasonal variability of the η' in the South China Sea. The monsoon is thought to be the primary force for the seasonal shift of the cold eddy and η' [16]. The seasonal variability of η'_{ULT} (second row in Figure 6) shows great similarity to η' , except that η'_{ULT} is smaller than η' in the northeastern South China Sea and larger than η' in the north central part of the South China Sea in winter. In summer and fall, η'_{ULT} is smaller than η' in the north central, northwestern and southern South China Sea. These differences can be clearly illustrated by the seasonal variability of η'_M (third row in Figure 6). Figure 7a shows the correlation coefficient between the monthly η' and η'_{ULT} . A significant positive correlation exists between 10°N and 15°N in the northeastern South China Sea, while in the north central, northwestern and southern South China Sea, the positive correlation is weak and even turns into a negative correlation in the north central and northwestern South China Sea. On the other hand,

the correlation coefficient between η' and η'_M (Figure 7b) is relatively high where the positive correlation between η' and η'_{ULT} is lower. Interestingly, the region where the higher positive correlation between η'_M and η'_M occurs is exactly the area where one can find the larger ratio of the standard deviation between η'_M and η'_{ULT} (Figure 7c), which shows the relative importance of these two components in the seasonal variability amplitude of η' . It can be concluded that the proportional relationship between η' and h'_1 is stronger and one can get an accurate ULT product based on Equation (14) between 10°N and 15°N and in the northeastern South China Sea. However, in the north central, northwestern and southern South China Sea, η'_M becomes important, and one must derive the ULT product according to Equation (16) instead of Equation (14).

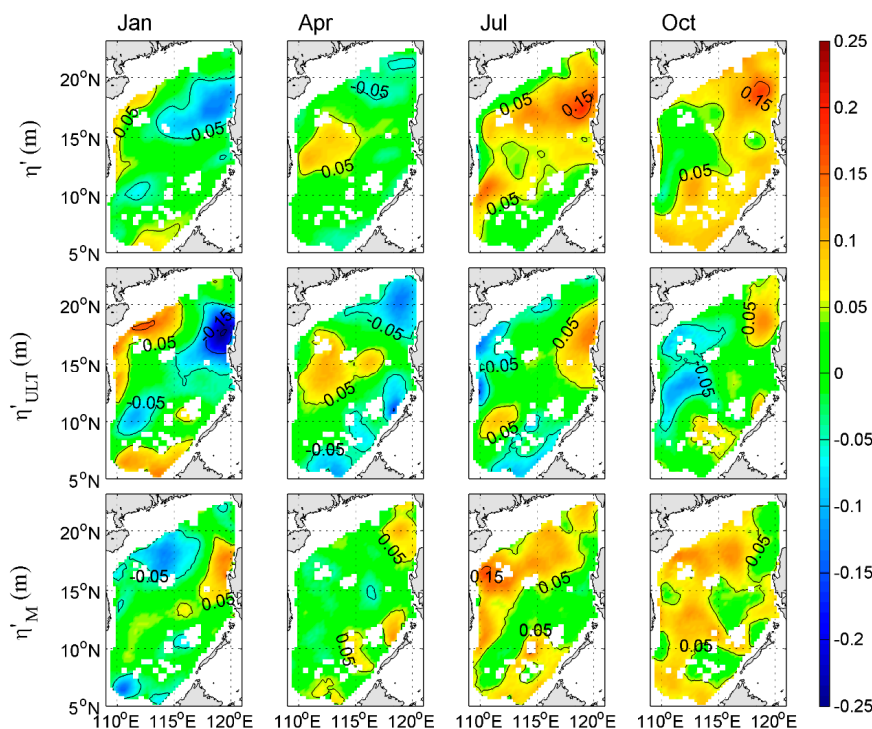


Figure 6. Seasonal variability of η' , η'_{ULT} and η'_M (CI: 0.1 m).

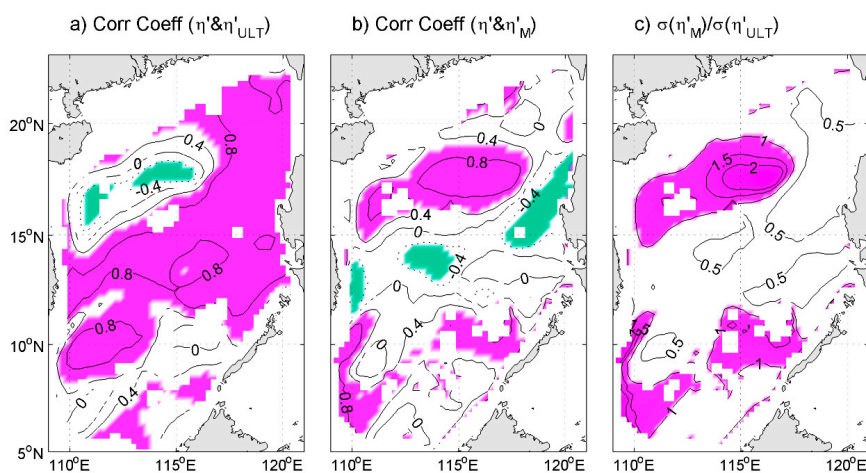


Figure 7. Spatial distributions of correlation coefficient between the monthly η' (a) with η'_{ULT} and (b) with η'_M . Shading in (a,b) indicates correlation beyond 95% confidence level; (c) The ratio of the standard deviation between η'_M and η'_{ULT} . The ratio larger than 1 is shaded in (c).

5. Product Evaluation

After identifying the parameters, one can easily get the altimeter-derived real-time ULT products based on Equations (14) and (16), respectively. These two products are compared and evaluated with different in situ observations.

The Argo-data-derived ULTs are directly obtained through computing the 25 kg/m^3 isopycnal depth at each Argo profile. Then the gridded altimeter-derived ULTs were interpolated to Argo profile locations to compare with the Argo-data-derived ULTs. The Argo measurements in the South China Sea are separated into the part north of 15°N and the part between 10°N and 15°N , because the relative importance of η'_{ULT} and η'_M is quite different in these two areas and the Argo data are very scarce in the southern South China Sea (Figure 2a). Figure 8 shows the comparison of the mean bias and root-mean-square error (RMSE) between the altimeter-derived and Argo-data-derived ULT in these two areas based on the two methods. Overall, the biases are positive, which indicate that the altimeter-derived products always overestimate the ULT directly calculated by the Argo observations. The overestimation can be somewhat reduced after considering η'_M . At the same time, the RMSE also achieves a certain degree of reduction. The bias and RMSE for the region north of 15°N are obviously larger than those between 10°N and 15°N . Specifically, without considering η'_M , the maximum bias ($\sim 12 \text{ m}$) and maximum RMSE (more than 15 m) can be found in summer and fall for the region north of 15°N . After adding η'_M , the bias is reduced to less than 3 m and the RMSE decreases by more than 27%. The situations are the same for the region between 10°N and 15°N , except that the bias and RMSE and the improvements after considering η'_M are relatively smaller than those north of 15°N . These results correspond to the large positive η'_M in summer and fall (third row in Figure 6) and prove the relative importance of η'_M in summer and fall, especially in the northern South China Sea. However, in winter and spring, the improvements are very limited after considering η'_M .

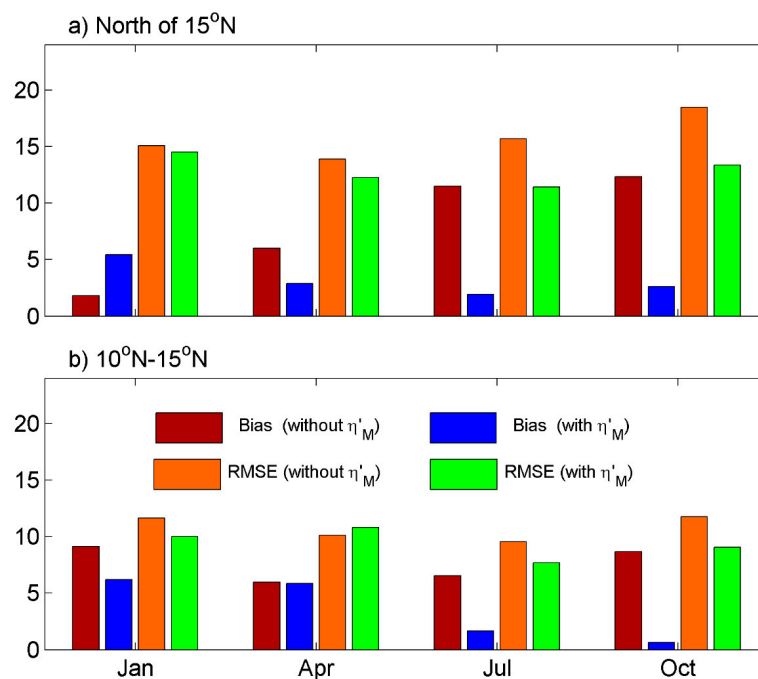


Figure 8. Bias and RMSE (Unit: m) between the altimeter-derived and Argo-data-derived ULT for the South China Sea (a) north of 15°N and (b) between 10°N and 15°N .

The CTD data collected during three joint cruises are used to validate the altimeter-derived ULT products. Figure 9 shows the differences between altimeter-derived and cruise-data-derived ULTs for these three cruises. The ULT differences at each station are derived in the same way as the

Argo profile. Results for the first two cruises are shown in the first two columns of Figure 9. They are during the summer and fall and cover nearly all the South China Sea. The altimeter-derived products, which neglect η'_M , evidently overestimate the cruise-data-derived ULT in these two cruises, especially in the north central, northwestern and southern South China Sea. After considering η'_M , the overestimations are substantially reduced, and the RMSE are reduced from 11.8 m and 14.5 m to 8.6 m and 11.7 m, respectively for the cruise in July 1998 and August 2000. The reduction rate of the RMSE for these two cruises is about 27% and 19%, respectively. However, both the altimeter-derived products underestimate the cruise-data-derived ULT off the southeast coast of Vietnam in August 2000 (second column in Figure 9). That may be because of the effects of an anticyclonic eddy, which is part of a dipole eddy pair associated with the summer eastward jet (e.g., [14,26,27,31,32]). The details still need further study. Furthermore, η'_M has a very limited influence on ULT products for the cruise in May 2004 (third column in Figure 9), and this agrees with previous studies that η'_M is very small (Figure 6) and the improvements are very limited after considering η'_M in spring (Figure 8b).

Next, we validate the two satellite-derived products with the data of the three ATLAS buoys in the South China Sea (Figure 10). The SCS1 is located in the northern South China Sea (Figure 1) where the relative importance of η'_M reaches its maximum (Figure 7c). The correlation coefficient and RMSE between the time series of ULT derived from the altimeter without considering η'_M and from the SCS1 is 0.54 and 15.2 m. The altimeter-derived product obviously overestimates the buoy-derived ULT during the summer and fall. Consistent with our expectations, these overestimations are markedly reduced after considering η'_M . The new product fits very well with the buoy-derived ULT, especially in summer and fall. The correlation coefficient rises to 0.81, and the RMSE decreases to 9.6 m. These results confirm the important role of η'_M in simulating the ULT in the northern South China Sea in summer and fall. For the buoys SCS2 and SCS3, when η'_M is neglected, the altimeter-derived products correspond well with the buoy-derived ULT. Their correlation coefficient is 0.91 and 0.69, and their RMSE is 9.7 m and 8.1 m for SCS2 and SCS3, respectively. After considering η'_M , the time series are basically the same (Figure 10b,c), which is consistent with the result that the effects of η'_M are smaller in the middle of the South China Sea (Figure 7c).

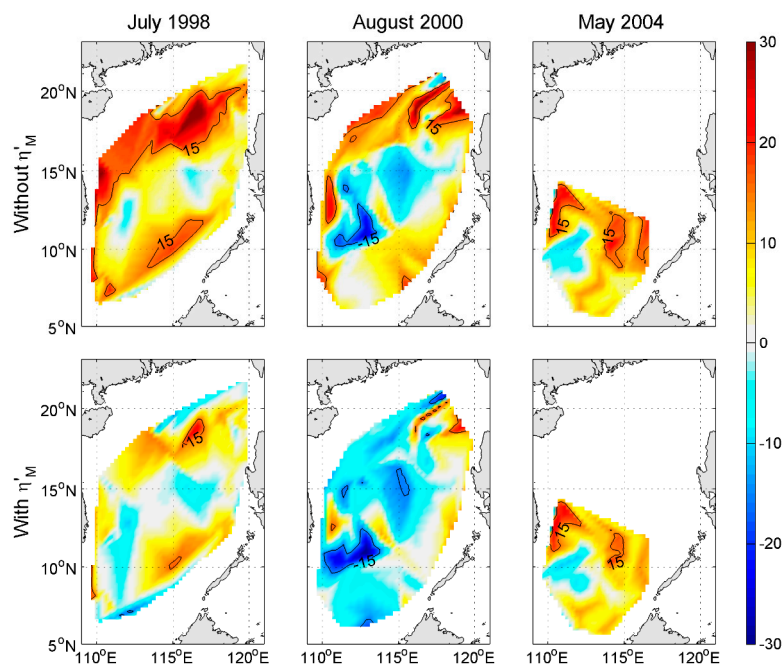


Figure 9. Spatial distribution of differences (Units: m) between altimeter-derived and cruise-data-derived ULT in July 1998 (**left**), August 2000 (**middle**) and May 2004 (**right**) without η'_M (**up**) and with η'_M (**down**).

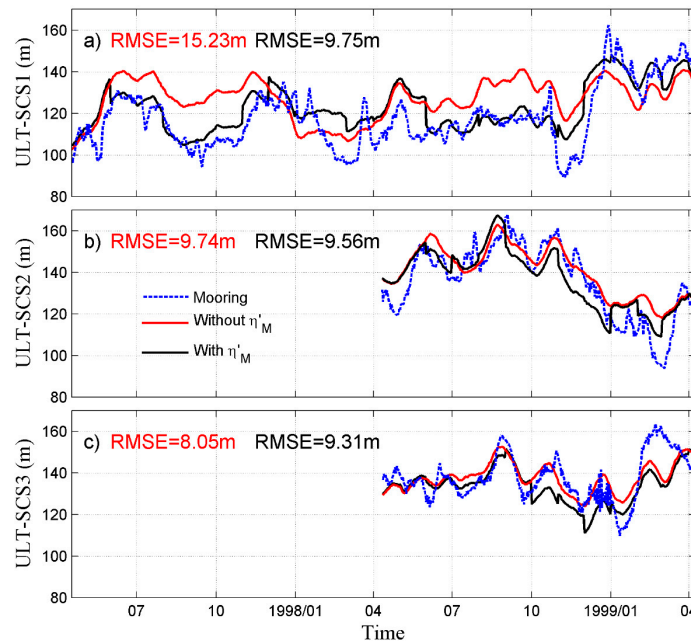


Figure 10. (a–c) Time series of buoy-data-derived ULT (blue dashed line), altimeter-derived ULT without η'_M (red solid line) and with η'_M (black solid line). The locations of three ATLAS buoys are marked in Figure 1.

6. Physical Mechanisms of the Modified Component

It is worth discussing the physical mechanisms that control η'_M . According to Gill and Niiler [11], the wind can affect η' in two ways: by changing the bottom pressure through barotropic motions and by changing the main thermocline through vertical Ekman pumping. In addition, the surface density flux can affect the near-surface steric height anomaly by changing the density in the mixed layer. Therefore, η'_{ULT} looks to be mainly under the control of baroclinic dynamics and η'_M is dominated by barotropic processes and the near-surface baroclinic thermodynamic processes. By comparing the 1.5-layer baroclinic planetary wave model and the barotropic Sverdrup model, Liu et al. [17] noted that the seasonal variability of η' in the South China Sea is mainly determined by surface wind curl on baroclinic Rossby waves and the barotropic contribution is very small. They also find that the surface steric height anomaly in the upper 50 m, which is controlled by surface heat flux forcing, contributes ~20% of the total steric height anomaly. According to Liu et al. [17], the surface steric height anomaly in the upper 50 m can be calculated as:

$$\eta'_{50} = -\frac{1}{\rho_0} \int_{-50\text{ m}}^0 \rho' dz, \quad (17)$$

in the same way as Equation (6). The differences between η'_s and η'_{50} represent the baroclinic dynamics component of η' , which is mainly correlated with the main thermocline variability. Liu et al. [17] also mentioned that the barotropic component of η' can be calculated by subtracting η'_s from the altimeter η' if both are exact.

Figure 11 shows the seasonal variability of the total steric height anomaly (η'_{WOA}), the surface steric height anomaly (η'_{WOA50}), and the baroclinic dynamics component of η' (η'_{WOAULT}) measured by the World Ocean Atlas 2013. Figure 11 also illustrates the seasonal variability of the barotropic component of η' (η'_{BT}) calculated by subtracting η'_{WOA} from η' (first row in Figure 6). The major seasonal features of η'_{WOA} and η'_{WOAULT} agree well with η' and η'_{ULT} (Figure 6), which suggests that the seasonal variability of the SLA is dominated by the baroclinic part, especially by the baroclinic dynamic processes. The seasonal variability of η'_{WOA50} is relatively small, and mainly manifests

as negative anomalies (smaller than -0.02 m) in winter and spring and positive anomalies (larger than 0.02 m) in summer and fall in the northern South China Sea. In the same way as Figure 7c, the relative importance of η'_{WOA50} , η'_{BT} , and η'_{WOAULT} is shown by comparing their standard deviation (Figure 12). From Figure 12a, η'_{WOA50} is found to be more important than η'_{WOAULT} only in the north central part of the South China Sea. This position is exactly where the buoy SCS1 is located and the maximum ratio of the standard deviation between η'_M and η'_{ULT} is found. This demonstrates that, in this region, the variability of η'_M can be partly explained as the effects of surface thermodynamic processes. The surface heat flux expands/contracts the water column in the mixed layer and brings a positive/negative η'_M in summer/winter, especially in the northern South China Sea. Comparing with η'_{WOA50} , η'_{BT} plays a more important role. η'_{BT} shows high positive values (larger than 0.05 m) in the northeastern South China Sea in winter, in the southern South China Sea in spring, and in the western South China Sea in summer and fall. The seasonal variability of η'_{BT} is the same as, but weaker than, η'_M . Besides the north central part of the South China Sea, the ratio of the standard deviation between η'_{BT} and η'_{WOAULT} is more than 1 in the northwestern and southern South China Sea (Figure 12b). After combining η'_{WOA50} and η'_{BT} , the ratio of the standard deviation between the combined effect and η'_{WOAULT} (Figure 12c) fits very well with that between η'_M and η'_{ULT} (Figure 7c). This confirms that η'_M is mainly under the control of the combined effect of surface thermodynamic and barotropic processes. However, whether the differences between η'_{WOA} and satellite-derived η' can represent the barotropic component is still open to discussion. The differences may also include the effects of the time inconsistency of these two datasets. The Gravity Recovery and Climate Experiment (GRACE) [33,34] will be included to discuss the seasonal variability of the barotropic component in future work.

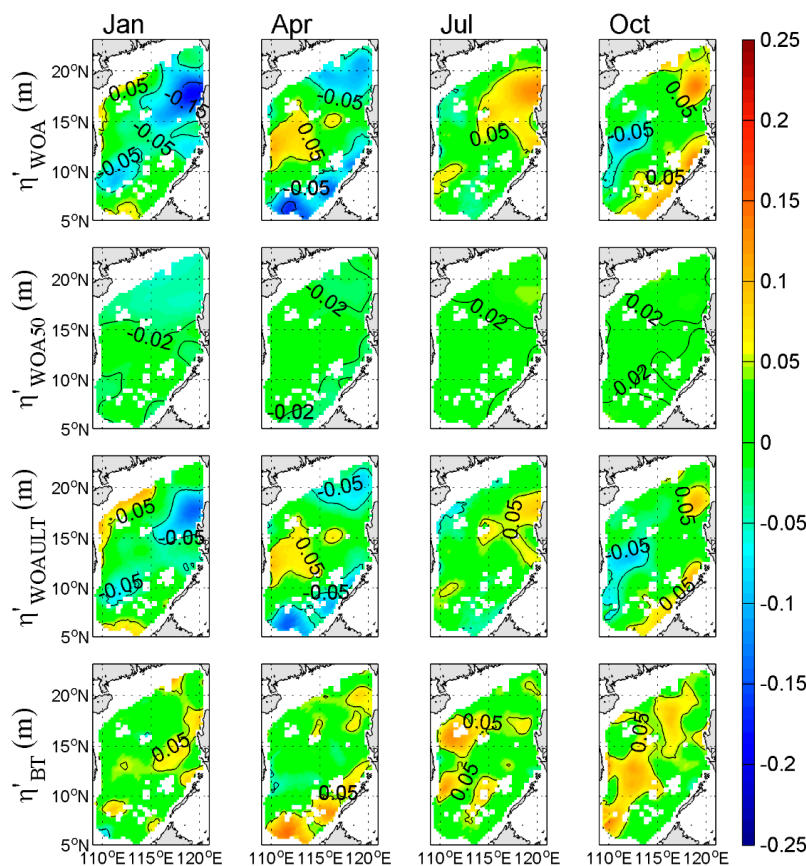


Figure 11. Seasonal variability of η'_{WOA} , η'_{WOA50} , η'_{WOAULT} and η'_{BT} .

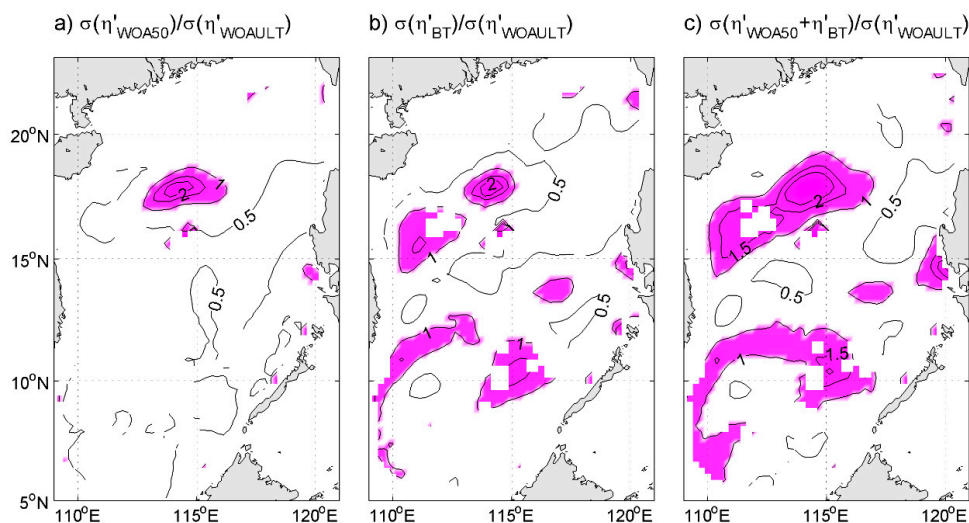


Figure 12. The ratio of the standard deviation (a) between η'_{WOA50} and η'_{WOAULT} ; (b) between η'_{BT} and η'_{WOAULT} ; and (c) between $\eta'_{WOA50} + \eta'_{BT}$ and η'_{WOAULT} . The ratio larger than 1 is shaded.

7. Conclusions and Discussion

The climatological monthly gridded temperature and salinity and SLA data are used to quantify the background field parameters of Equations (14) and (16) based on a highly simplified two-layer ocean model. The first method considers that the SLA is directly proportional to the ULTA, and the other separates SLA into two parts: the component proportional to ULTA, η'_{ULT} , and the modified component η'_M , which can correct the difference between η' and η'_{ULT} introduced by other physical processes. With these equations, one can derive two real-time ULT products using the SLA data. As far as we know, this is the first time to have obtained the altimeter-derived ULT products with gridded World Ocean Atlas 2013 data. Compared to the former products ($2^\circ \times 2^\circ$) derived from the site data (e.g., [10]), the new products have higher resolution ($0.25^\circ \times 0.25^\circ$) and thus can identify the ULT structures at smaller scales.

The 25 kg/m^3 isopycnal depth is chosen as the representation of the ULT after comparing different choices. The alternative choice is the 20°C isotherm depth due to the salinity effect being weak. In the South China Sea, the mean ULT is $\sim 120 \text{ m}$, and there are two obvious eddy-like thinner ULT areas corresponding to two cold eddies. The mean reduced gravity is $\sim 0.073 \text{ m/s}^2$, which is about one order of magnitude larger than the value obtained in the open deep ocean. Both η' and η'_{ULT} display a clear seasonal variability and their variability shows great similarity, except in the north central, northwestern and southern South China Sea, where the η'_M has higher correlation with η' and larger standard deviation relative to η'_{ULT} .

Three different in situ observations are used to compare and evaluate these two ULT products. Both the high-resolution altimeter-derived products satisfactorily simulate the ULT in the South China Sea. The range of the RMSE is from less than 10 m to $\sim 15 \text{ m}$ in different evaluations. The monthly varied η'_M is firstly introduced into the two-layer ocean model. We found that η'_M is really necessary to correct the overestimation in summer and fall reported by the altimeter-derived ULT product without considering η'_M , especially in the northern South China Sea. However, in winter and spring, and in the middle South China Sea, the corrective action of η'_M is limited. Nevertheless, it is comforting to see that the bias and RMSE is relatively small in these situations even if without η'_M . The in situ observations in the South China Sea south of 10°N were too few to evaluate the satellite-derived ULT product. Finally, the physical mechanisms of η'_M are found to be mainly under the control of the combined effect of barotropic and surface thermodynamic processes.

Acknowledgments: This research was supported by the National Key R&D Program of China (grant 2016YFA0601804 and 2016YFA0601803), National Science Foundation of China (grant 41606021, 41606017, and 41476022), Open Fund of State Key Laboratory of Satellite Ocean Environment Dynamics (grant QNHX1610), the Startup Foundation for Introducing Talent of NUIST (grant 2014r017 and 2014r072), the National Program on Global Change and Air-Sea Interaction (grant GASI-03-IPOVAI-05), and the Priority Academic Program Development of Jiangsu Higher Education Institutions (PAPD). The authors would like to thank Gregory P. King for language editing. The authors also thank South China Sea Institute of Oceanology of the Chinese Academy of Sciences for supplying the ATLAS buoys' data during the South China Sea Monsoon Experiment and the CTD probe data of the joint cruise investigations.

Author Contributions: D.W. and C.D. conceived and designed the experiments; Y.C., K.Y., Z.H. and Y.Y. performed the experiments; Y.C. and K.Y. analyzed the data; Y.C. wrote the paper. K.Y. and Y.Y. helped modify the manuscript.

Conflicts of Interest: The authors declare no conflict of interest.

References

- Goni, G.J.; Kamholz, S.; Garzoli, S.L.; Olson, D.B. Dynamics of the Brazil-Malvinas confluence based on inverted echo sounders and altimetry. *J. Geophys. Res.* **1996**, *101*, 16273–16289. [[CrossRef](#)]
- Garzoli, S.L.; Goni, G.J.; Mariano, A.J.; Olson, D.B. Monitoring the upper southeastern Atlantic transports using altimeter data. *J. Mar. Res.* **1997**, *55*, 453–481. [[CrossRef](#)]
- Sainz-Trapaga, S.; Goni, G.J.; Sugimoto, T. Identification of the Kuroshio Extension, its bifurcation and Northern Branch from altimetry and hydrographic data during October 1992–August 1999: Spatial and temporal variability. *Geophys. Res. Lett.* **2001**, *28*, 1759–1762. [[CrossRef](#)]
- Goni, G.J.; Wainer, I. Investigation of the Brazil current front variability from altimeter data. *J. Geophys. Res.* **2001**, *106*, 31117–31128. [[CrossRef](#)]
- Shay, L.K.; Goni, G.J.; Black, P.G. Effects of a warm oceanic feature on Hurricane Opal. *Mon. Weather Rev.* **2000**, *128*, 1366–1383. [[CrossRef](#)]
- Pun, I.F.; Lin, I.I.; Wu, C.R.; Ko, D.S.; Liu, W.T. Validation and application of altimetry derived upper ocean thermal structure in the western North Pacific Ocean for typhoon intensity forecast. *IEEE Trans. Geosci. Remote Sens.* **2007**, *45*, 1616–1630. [[CrossRef](#)]
- Polito, P.S.; Sato, O.T. Patterns of sea surface height and heat storage associated to intraseasonal Rossby waves in the tropics. *J. Geophys. Res.* **2003**, *34*, L09603. [[CrossRef](#)]
- Lentini, C.A.D.; Goni, G.J.; Olson, D.B. Investigation of Brazil current rings in the confluence region. *J. Geophys. Res.* **2006**, *111*. [[CrossRef](#)]
- Momin, I.M.; Sharma, R.; Basu, S. Satellite-derived heat content in the tropical Indian Ocean. *Remote Sens. Lett.* **2011**, *2*, 269–277. [[CrossRef](#)]
- Lin, C.Y.; Ho, C.R.; Zheng, Z.W.; Kuo, N.J. Validation and variation of upper layer thickness in South China Sea from satellite altimeter data. *Sensors* **2008**, *8*, 3802–3818. [[CrossRef](#)] [[PubMed](#)]
- Gill, A.E.; Niiler, P.P. The theory of seasonal variability in the ocean. *Deep Sea Res.* **1973**, *20*, 141–177. [[CrossRef](#)]
- Wyrtki, K. Scientific Results of Marine Investigations of the South China Sea and the Gulf of Thailand. In *Physical Oceanography of the Southeast Asian Waters*; Scripps Institution of Oceanography: La Jolla, CA, USA, 1961; Volume 2, p. 195.
- Qu, T. Upper-Layer Circulation in the South China Sea. *J. Phys. Oceanogr.* **2000**, *30*, 1450–1460. [[CrossRef](#)]
- Liu, Y.; Weisberg, R.H.; Yuan, Y. Patterns of upper layer circulation variability in the South China Sea from satellite altimetry using the self-organizing map. *Acta Oceanol. Sin.* **2008**, *27*, 129–144. [[CrossRef](#)]
- Amiruddin, A.; Haigh, I.; Tsimplis, M.; Calafat, F.; Dangendorf, S. The seasonal cycle and variability of sea level in the South China Sea. *J. Geophys. Res.* **2015**, *120*, 5490–5513. [[CrossRef](#)]
- Cheng, Y.; Hamlington, B.; Plag, H.-P.; Xu, Q. Influence of ENSO on the variation of annual sea level cycle in the South China Sea. *Ocean Eng.* **2016**, *126*, 343–352. [[CrossRef](#)]
- Liu, Z.; Yang, H.; Liu, Q. Regional dynamics of seasonal variability in the South China Sea. *J. Phys. Oceanogr.* **2001**, *31*, 272–284. [[CrossRef](#)]
- Cheng, X.; Qi, Y. On steric and mass-induced contributions to the annual sea-level variations in the South China Sea. *Glob. Planet Chang.* **2010**, *72*, 227–233. [[CrossRef](#)]
- World Ocean Atlas 2013. Available online: <http://apdrc.soest.hawaii.edu> (accessed on 4 March 2017).

20. Archiving, Validation and Interpretation of Satellite Oceanographic Data. Available online: <ftp.avisio.altimetry.fr> (accessed on 4 March 2017).
21. Le Traon, P.Y.; Ogor, F. ERS-1/2 orbit improvement using TOPEX/POSEIDON: The 2 cm challenge. *J. Geophys. Res.* **1998**, *103*, 8045–8057. [[CrossRef](#)]
22. Le Traon, P.Y.; Nadal, F.; Ducet, N. An improved mapping method of multisatellite altimeter data. *J. Atmos. Ocean. Technol.* **1998**, *15*, 522–534. [[CrossRef](#)]
23. US Global Ocean Data Assimilation Experiment. Available online: http://www.usgodae.org/cgi-bin/argo_select.pl (accessed on 4 March 2017).
24. Liu, Y.; Yuan, Y.; Su, J.; Jiang, J. Circulation in the South China Sea in summer of 1998. *Chin. Sci. Bull.* **2000**, *45*, 1648–1655. [[CrossRef](#)]
25. Zeng, L.; Wang, D.; Chen, J.; Wang, W.; Chen, R. SCSPOD14, a South China Sea physical oceanographic dataset derived from in situ measurements during 1919–2014. *Sci. Data* **2016**, *3*, 160029. [[CrossRef](#)] [[PubMed](#)]
26. Metzger, E.J.; Hurlburt, H. Coupled dynamics of the South China Sea, the Sulu Sea, and the Pacific Ocean. *J. Geophys. Res.* **1996**, *101*, 12331–12352. [[CrossRef](#)]
27. Wang, G.; Chen, D.; Su, J. Generation and life cycle of the dipole in the South China Sea summer circulation. *J. Geophys. Res.* **2006**, *111*, C06002. [[CrossRef](#)]
28. Zhuang, W.; Qiu, B.; Du, Y. Low-frequency western Pacific Ocean sea level and circulation changes due to the connectivity of the Philippine Archipelago. *J. Geophys. Res.* **2013**, *118*, 6759–6773. [[CrossRef](#)]
29. He, Y.; Cai, S.; Wang, D.; He, J. A model study of Luzon cold eddies in the northern South China Sea. *Deep Sea Res. Part I* **2015**, *97*, 107–123. [[CrossRef](#)]
30. Gan, J.; Qu, T. Coastal jet separation and associated flow variability in the southwest South China Sea. *Deep Sea Res. Part I* **2008**, *55*, 1–19. [[CrossRef](#)]
31. Wu, C.R.; Shaw, P.T.; Chao, S.Y. Assimilating altimetric data into a South China Sea model. *J. Geophys. Res.* **1999**, *104*, 29987–30005. [[CrossRef](#)]
32. Chu, X.; Xue, H.; Qi, Y.; Chen, G.; Mao, Q.; Wang, D.; Chai, F. An exceptional anticyclonic eddy in the South China Sea in 2010. *J. Geophys. Res.* **2014**, *119*, 881–897. [[CrossRef](#)]
33. Chambers, D.P.; Bonin, J.A. Evaluation of Release 05 time-variable gravity coefficients over the ocean. *Ocean Sci.* **2012**, *8*, 859–868. [[CrossRef](#)]
34. Chambers, D.P.; Willis, J.K. A Global Evaluation of Ocean Bottom Pressure from GRACE, OMCT, and Steric-Corrected Altimetry. *J. Atmos. Ocean Technol.* **2010**, *27*, 1395–1402. [[CrossRef](#)]



© 2017 by the authors. Licensee MDPI, Basel, Switzerland. This article is an open access article distributed under the terms and conditions of the Creative Commons Attribution (CC BY) license (<http://creativecommons.org/licenses/by/4.0/>).